Ionic liquid ferrofluid electrospray

A new satellite propulsion system

Author:
Stephan den Hartog

Supervisors:
Dr. Ben Erne
Prof. Dr. Lyon King

November 2015
Ion Space Propulsion Laboratory
Michigan Technological University, USA

Abstract

An electrospray array consisting of an ionic liquid ferrofluid was designed and investigated. When subjected to a magnetic field, the ferrofluid forms peaks on the surface called Rosensweig instabilities. By applying a sufficiently strong electric field, electrospray can be obtained from these peaks. A reservoir consisting of concentric ring trenches was designed and constructed in order to facilitate the formation of a uniform array of ILFF peaks. It was found that the array of peaks could be made relatively uniform in shape and size. Emission measurements were performed on these arrays to determine whether uniform emission could be obtained from the array. Relatively uniform emission was confirmed in several experiments from seven or eight peaks simultaneously.

Table of contents

1. Introduction

1.1 Propulsion systems for satellites

Modern day society relies heavily on the use of satellites – for example for communication, GPS and weather tracking – and, like all electronic devices, satellites are becoming smaller and smaller. A recent example is the development of the CubeSat[1], a small satellite consisting of several small standard units of 10x10x10 cm^3 (Fig. 1.1). CubeSats and other types of small satellites have a cost advantage over bigger satellites. They are cheaper to produce and are less costly to send in an orbit around the Earth, because a higher number of small satellites can be launched in a single rocket.

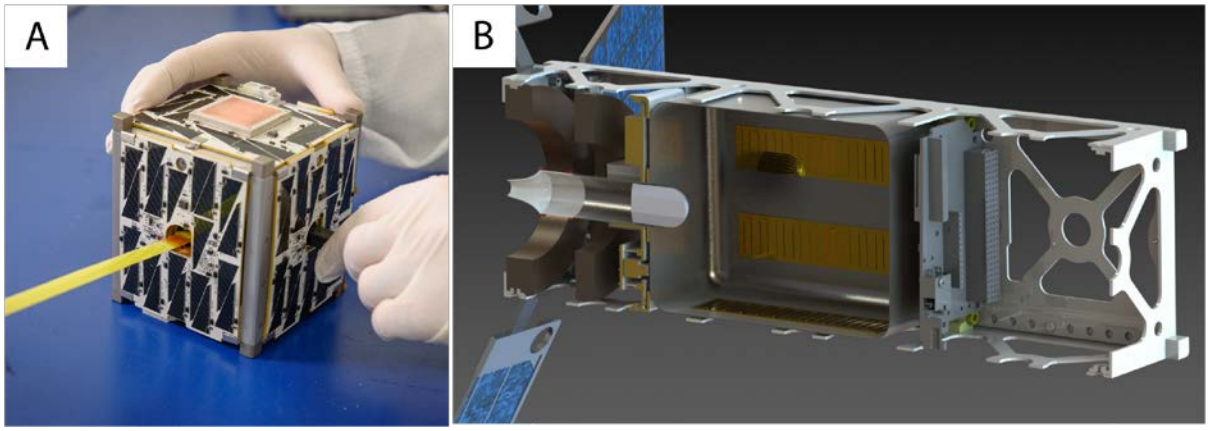

Figure 1.1: A) An image of a single CubeSat unit being constructed at NASA. One unit, dubbed 'U', has the dimensions 10x10x10 cm^3. B) A computer generated image of a CubeSat frame. Most CubeSats are comprised of a frame designed to hold three U's. (Image courtesy: NASA, University of Michigan)

Satellites in low Earth orbit experience significant drag from small atmospheric particles and thus require a means of propulsion to adjust their orbit or execute small course corrections. Since satellites have a limited amount of fuel, a satellite's lifetime is mostly determined by the efficiency of its propulsion system. At the moment, two types of space propulsion exist: chemical engines and ion thrusters, shown in Figure 1.2. Chemical engines propel a spacecraft by the combustion of a mono- or bipropellant. Such engines provide high thrust (10^1 - 10^7 N), but generally have a low efficiency. This makes them a good choice for sending payloads into orbit or in-space propulsion systems for heavy spacecraft. Ion thrusters expel ions at high velocity to provide low thrust (10^{-6} - 10^{-3} N) with high efficiency[2,3]. This makes them the preferred choice for medium-sized

satellites, since they can function for a long time and produce sufficient thrust for such spacecraft if fired for a long enough period of time.

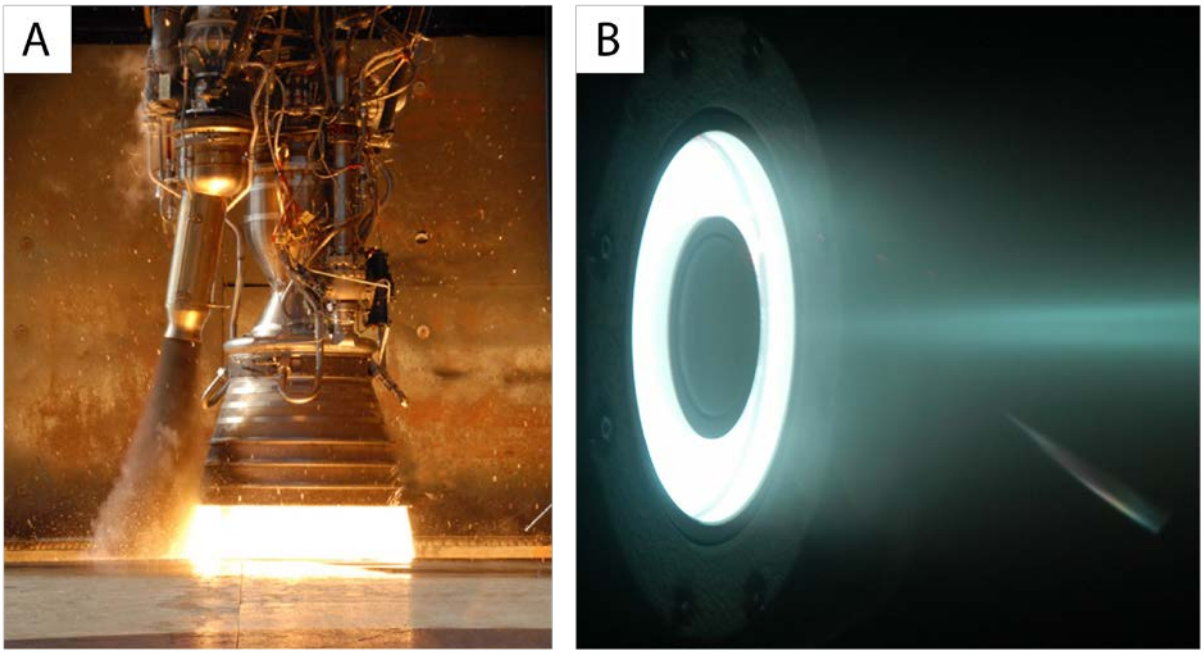

Figure 1.2: A) Chemical combustion engines such as the Merlin 1C by SpaceX produce tremendous amounts of thrust, but are inefficient. B) Ion engines such as this Hall effect thruster being tested at NASA Glenn Research Centre deliver low thrust at a very high efficiency. (Image courtesy: SpaceX, NASA Glenn Research Centre)

However, current ion thrusters such as the Hall effect thruster used on the "Dawn" spacecraft to Ceres[4] cannot be scaled down to CubeSat size or become too inefficient if scaled down. Industry and research groups have been developing alternative forms of propulsion such as plasma thrusters, resistojets and electrospray thrusters[5,6,7,8]. The latter option has attracted attention due to its high fuel efficiency, small size and relative simplicity.

1.2 Electrospray thrusters

Electrospray thrusters use an electric field to emit ions and/or charged particles from a liquid fuel[9]. The emitted ions or particles are accelerated by the electric field to provide thrust. The liquid propellant must be polar or conductive and can be either an ionic liquid or a liquid metal[10]. Ionic liquids have the benefit of requiring a weaker electric field to emit than liquid metal, but must have a low vapour pressure to prevent evaporation of the liquid to the vacuum of space. A single electrospray emitter only provides several nanonewtons of thrust[3], which is not enough to propel a CubeSat within a reasonably period of time. Electrospray thrusters are therefore comprised of

arrays of a support structure, usually a capillary or a needle[11,12]. An image of a commercial electrospray thruster is shown in Figure 1.3a. The electric field is created by applying a voltage potential between the support structure and an extraction electrode. The liquid at the tip of the capillary or needle is drawn towards the electrode as the voltage potential is increased. At the onset voltage, usually on the order of several kilovolts, the liquid forms a Taylor cone and emission starts from the apex of this cone. Each capillary or needle functions as a single emitter, with an array of $\pm 10^3$ capillaries or needles providing enough thrust for a CubeSat[7].

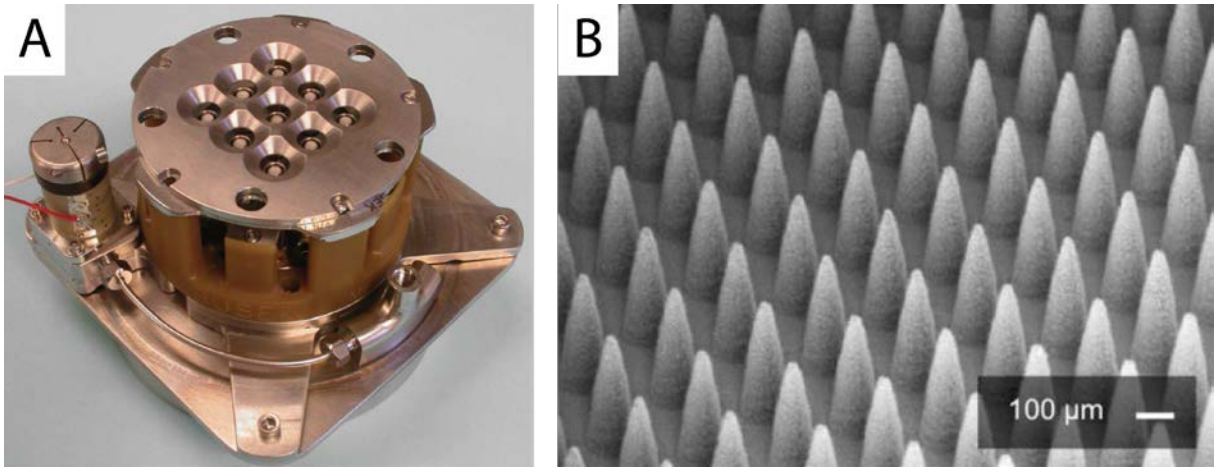

Figure 1.3: A) Commercial electrospray thrusters are starting to enter the market. These devices are made of arrays of small needles that function as a support structure. B) An array of needles prepared by etching. (Image courtesy: BuSEK Co. Inc., Massachussets Institute of Technology)

The arrays are typically fabricated using wet etching or photolithography, which is a time-consuming process that can require weeks and may yield non-uniform emitter tips[13]. Figure 1.3b shows an image of an array created via etching. The resulting arrays tend to be quite fragile and are easily damaged during handling or transport – especially during the violent process of sending a rocket into space. Arcing and other catastrophic events can severely damage the capillaries or needle tips. The support structure is also susceptible to degradation due to ion bombardment. A new type of propellant based on ionic liquid ferrofluid (ILFF) shows promise as an alternative to capillary arrays[14]. The ferrofluid forms peaks called Rosensweig instabilities in the presence of a magnetic field, which replace the support structure of traditional electrospray arrays. Because the ferrofluid is based on an ionic liquid, each of the peaks can function as an electrospray source when a sufficiently high electric field is applied. The liquid forms peaks when exposed to the magnetic field within seconds and peaks repair themselves when

damaged by simply realigning to the field. Previous work on ILFF electrospray emitters by E.J. Meyer[14,15] has shown that electrospray can be observed from both a single peak emitter and a five-peak emitter. He showed that two different ILFFs could be used as an electrospray source and that damage to the array was quickly repaired.

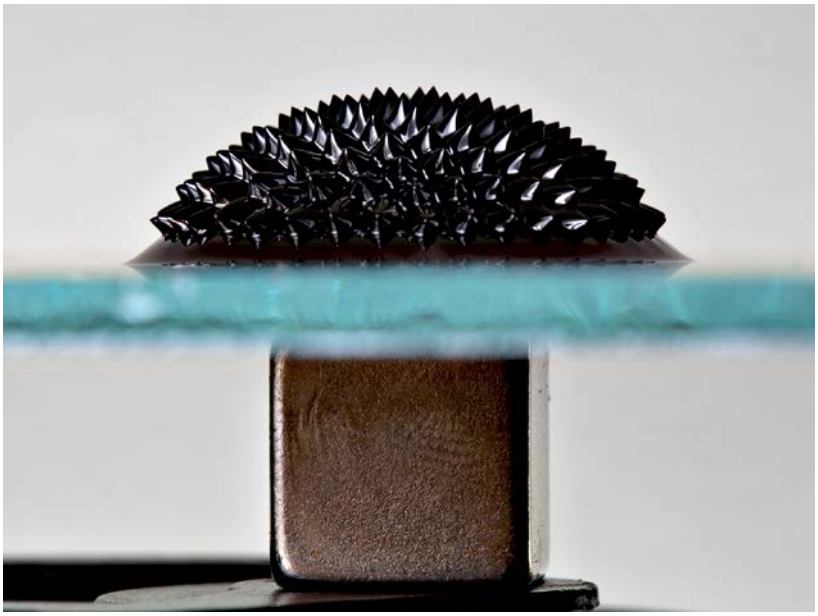

Figure 1.4: An image of a pool of ferrofluid suspended above a magnet. The peaks that are formed are called Rosensweig instabilities and can used as an electrospray support structure. (Image courtesy: Wikipedia)

1.3 Project goals

The goal of this project was to design and build a working multi peak ILFF emitter array and identifying any difficulties in building and operating such an array. This research is divided into two parts: the design and build phase of a multi peak ILFF array (1) and achieving uniform electrospray emission from this array (2). The design phase encompassed various ILFF reservoirs of different geometries as well as different magnet configurations. The final design was incorporated in a setup designed to measure the emission current from the electrospray source. An ILFF based on 1-ethyl-3-methylimidazolium bis(trifluoromethylsulphonyl)imide (EMIm-NTf2) with ±25% magnetic Fe_2O_3 nanoparticles was used as an electrospray fuel. Current/voltage measurements were performed to determine emission characteristics of the electrospray array.

2. Theory

2.1 Electrospray

Electrospray is the ejection of ions and/or charged particles from a polar or conductive liquid due to the presence of a sufficiently high electric field. The history of electrospray is older than one might expect. The first experiments on electrospray were performed in the 18th century when Jean-Antoine Nollet noted that water flowing from a container would aerosolize when the container was connected to a high-voltage power source[16]. Two centuries later Zeleny published a paper on the disintegration of water droplets emerging from a capillary due to the application of a high voltage potential[17]. He was the first one to image the droplets that were emitted from the tip apex. It was not until Taylor derived the theoretical groundwork for the formation of this tip apex that research on electrospray took off[18]. It was initially deemed important for the investigation of thunderclouds, but the field quickly expanded and nowadays electrospray is used in various techniques such as mass spectrometry, electrospinning and focused ion beams[19,20,21].

A simple electrospray source is shown in Figure 2.1. A high voltage potential is applied across a capillary containing a conductive liquid and an extractor electrode. At a certain threshold value called the 'onset voltage' electrospray occurs from the tip apex or 'Taylor cone' and ions and/or charged particles are ejected from the liquid.

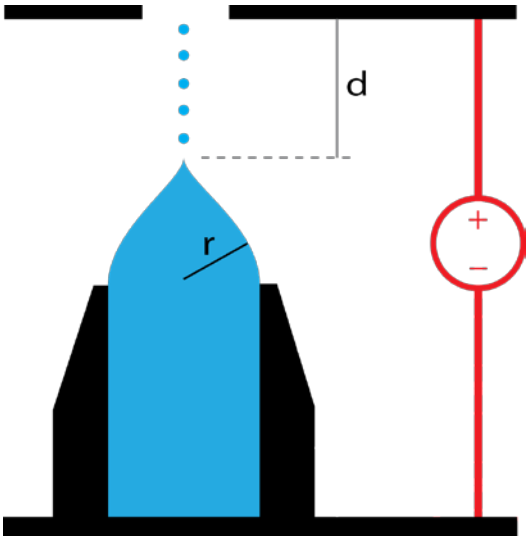

Figure 2.1: An illustration of a typical electrospray emitter. A conductive or polar liquid is wetted on a capillary needle so that the fluid has a small meniscus with radius r. A sufficiently high electric field is applied between the fluid and an extractor plate at distance d so that the fluid starts emitting ions and/or charged particles.

The formation of a Taylor cone can be understood by determining the balance of electric and surface stresses across a liquid interface. An image of such an interface is shown in Figure 2.2. The electric stress across the liquid surface is given by equation 2.1:

$$\sigma_E = \left(\varepsilon_0 E_{n,0}^2 - \frac{1}{2}\varepsilon_0 E_{n,0}^2\right) - \left(\varepsilon_0 \varepsilon_R E_{n,1}^2 - \frac{1}{2}\varepsilon_0 E_{n,1}^2\right) \qquad \textit{Equation 2.1}$$

where ε_0 is the vacuum permittivity, ε_R is the relative permittivity of the liquid, $E_{n,0}$ is the normal vacuum electric field and $E_{n,1}$ is the normal liquid electric field. The electric field normal to the surface must be continuous and is given by:

$$\varepsilon_0 E_{n,0} = \varepsilon_0 \varepsilon_R E_{n,1} \qquad \textit{Equation 2.2}$$

By combining equations 2.1 and 2.2 and assuming the electric field is applied normal to the surface, an expression for the electric stress can be obtained:

$$\sigma_E = \frac{1}{2}\varepsilon_0 E^2 \left(1 - \frac{2}{\varepsilon_R} + \frac{1}{\varepsilon_R^2}\right) \qquad \textit{Equation 2.3}$$

The relative permittivity can be as high as 90.0 for certain ionic liquids, but most ionic liquids have values ranging between 10.0 and 20.0. The ionic liquid used in this research, EMIm-NTf2, has a relative permittivity of 12.0. This reduces equation 2.3 to:

$$\sigma_E = 0.42\varepsilon_0 E^2 \qquad \textit{Equation 2.4}$$

Electrospray occurs when the electric stress caused by the electric field is in equilibrium with the surface tension stress that is given by equation 2.5:

$$\sigma_S = \frac{2\gamma}{r} \qquad \textit{Equation 2.5}$$

Here, γ is the liquid surface tension and r is the radius of the fluid meniscus. The electric field is proportional to the applied voltage potential and is uniform across the meniscus. However, as the hemispherical meniscus starts to deform into a cone shape due to the electric stress, the electric field is enhanced near the tip. Prewett and Mair[21] described this enhanced electric field near the tip apex to be:

$$E = \frac{2V}{r \ln\frac{2d}{r}} \qquad \textit{Equation 2.6}$$

where d is the distance between the tip and the extractor electrode, V is the applied voltage potential and r is the radius of curvature of the tip. By combining equations 2.4, 2.5 and 2.6 an expression for the onset voltage is obtained:

$$V = \ln\frac{2d}{r}\sqrt{\frac{\gamma r}{\varepsilon_0}} \qquad \textit{Equation 2.7}$$

It is preferable to have a low onset voltage, since this would require less power to operate an electrospray thruster. Because of this, ionic liquids are preferred over liquid metals: liquid metals have a very high surface tension and require more power to eject ions or particles. To give the fluid a small radius of curvature, it is wetted onto a capillary or needle support. In the case of ILFF, the Rosensweig instability that is formed in a magnetic field provides the support structure. Meyer found that the observed onset voltage for ILFF emitters based on EMIm-NTf2 was 16-24% lower than the calculated value[15]. This is most likely because equation 2.7 does not take any magnetic stresses on the fluid into account.

2.2 Ferrofluids

Ferrofluids are fluids consisting of single domain superparamagnetic nanoparticles suspended in a carrier liquid. The nanoparticles are made of a ferromagnetic material such as iron oxide and generally have a size of around 10 nm. Their small size makes the particles susceptible to Brownian motion and prevents sedimentation due to gravity[22].

The particles are coated in a surfactant to prevent particle clustering (Fig. 2.2). The surfactant usually consists of an organic molecule with a polar and a non-polar part.

Depending on the carrier liquid, either the polar or the non-polar part of the surfactant molecule is attached to the nanoparticle. The electrostatic or steric repulsion between the surfactant tails prevents clustering of the coated particles.

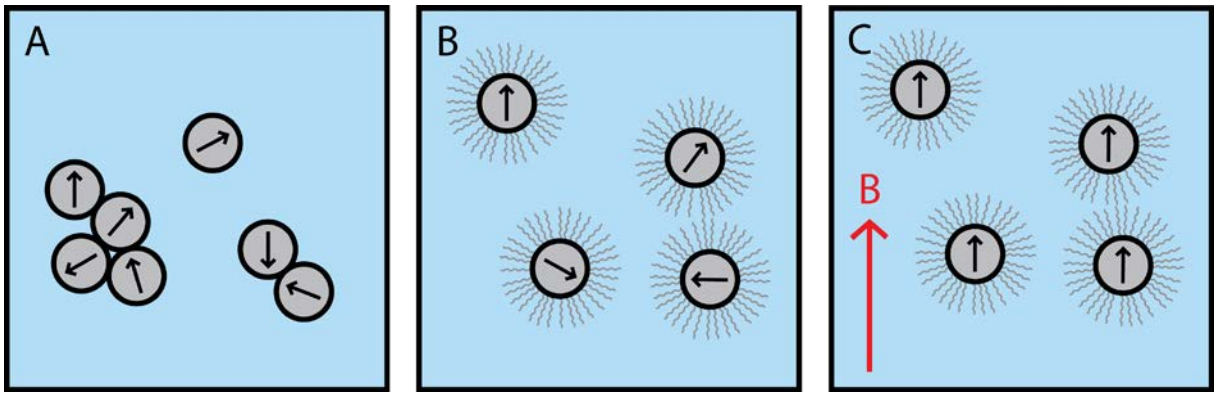

Figure 2.2: A) Fe_2O_3 nanoparticles suspended in a carrier liquid have single magnetic domains that are oriented randomly. Uncoated nanoparticles tend to cluster together to minimize their surface energy. B) To prevent clustering, the particles are coated with surfactant molecules that repel each other electrostatically or sterically. C) When a magnetic field is applied the particles align with the field.

The carrier liquid can be any non-magnetic liquid: water-based, oil-based and even mercury-based ferrofluids are available. Recently, ferrofluids have also been prepared from ionic liquids[23]. This type of ferrofluid has the benefit of being both susceptible to magnetic fields and conductive. The susceptibility of a ferrofluid to a magnetic field depends on the concentration of superparamagnetic nanoparticles. Typically, a ferrofluid contains around 15-25% w/w of nanoparticles[22]. When a volume of ferrofluid with a free surface is exposed to a sufficiently strong magnetic field, peaks called 'Rosensweig instabilities' appear on the surface. The peaks align parallel to the magnetic field and form a symmetrical grid on the surface.

2.3 Rosensweig instabilities

The formation of a Rosensweig peak is caused by a small non-uniformity near the free surface of the ferrofluid. Figure 2.3 shows the formation of a Rosensweig instability. As the surface starts to deform, the magnetic field is focused at this deformation. The focusing of the magnetic field causes the deformation to grow even further, until it is stabilised by the counterbalance of gravitational and surface energies. The stable peaks that are formed are the result of the minimalization of the total magnetic, surface and gravitational energies.

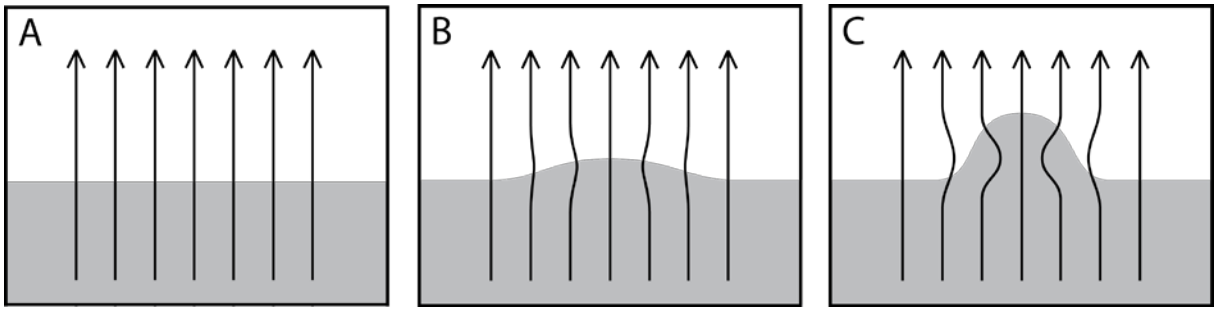

Figure 2.3: An illustration of the formation of a Rosensweig instability in a magnetic field. A) Initially, no peak forms. B) However, due to a slight non-uniformity, the surface starts to deform. The field is focused at this deformation. C) Due to the focusing of the field, the deformation grows further until an equilibrium between magnetic, gravitational and surface energies is achieved.

Rosensweig was the first to provide a full theoretical underpinning for modelling Rosensweig instabilities[24]. He assumed that the fluid was incompressible and inviscid, and that Gauss' and Ampere's Laws held. As such, the motion of a magnetic fluid can be described using the Navier-Stokes equation:

$$\rho\left(\frac{\partial \vec{v}}{\partial t} + \vec{v}\cdot\nabla\vec{v}\right) = -\nabla(p + \rho g z) \qquad \textit{Equation 2.8}$$

where ρ is the fluid density, p is the pressure, g is gravitational acceleration and z is the fluid height. The pressure balance across the fluid-vacuum interface can be written as:

$$p + \frac{1}{2}\mu_0 M_n^2 + \mu_0 \int_0^H M dH - 2\gamma \text{H} = 0 \qquad \textit{Equation 2.9}$$

where v is the fluid velocity, μ_0 is the permeability of free space, M_n is the magnetization normal to the fluid surface, μ_R is the fluid permeability, M is the fluid magnetization, H is the magnetic field, γ is the fluid surface tension and H is the fluid mean curvature. The surface shape is assumed to be a simple periodic wave:

$$z \propto e^{-i(\omega t - \vec{k}r)} \qquad \textit{Equation 2.10}$$

where ω is the wave frequency, k is the wave number and r is the position on the surface. When equations 2.8 – 2.10 are combined and perturbation theory is applied, the dispersion relation for the fluid can be found:

$$\rho\omega^2 = \rho g k + \gamma k - \frac{k^2\mu_0 M^2}{1+\frac{1}{\mu_r}} \qquad \textit{Equation 2.11}$$

The Rosensweig instability forms when $\omega^2 = 0$ and $\delta\omega/\delta k = 0$. If ω is real, the surface amplitude shrinks, whether if ω is imaginary, the surface amplitude grows. At $\delta\omega/\delta k = 0$

the dominant or critical wave number k_c can be determined, from which the critical value of magnetization M_c can be found:

$$k_c = \sqrt{\frac{\rho g}{\gamma}} \qquad \textit{Equation 2.12}$$

$$M_c^2 = \frac{2}{\mu_0}\left(1 + \frac{1}{\mu_r}\right)\sqrt{\rho g \gamma} \qquad \textit{Equation 2.13}$$

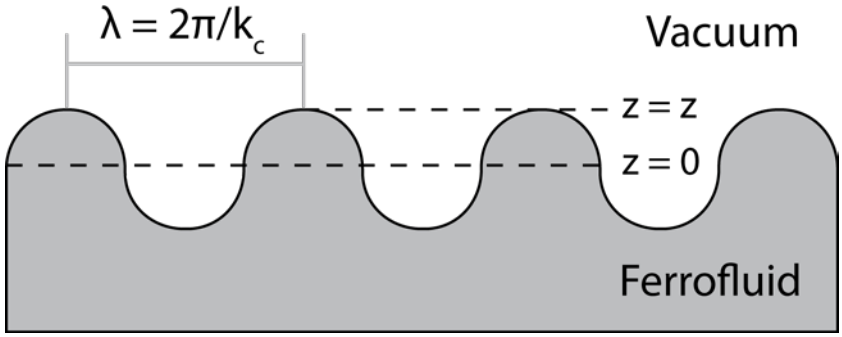

Figure 2.4: The Rosensweig peaks can be modelled as a simple surface wave, where the height of the peaks is given by the wave amplitude z. The peak-to-peak spacing is given by the wavelength λ.

From equation 2.12, the peak-to-peak spacing can be determined. While this theory holds for uniform magnetic fields, it is not applicable to non-uniform fields. For non-uniform magnetic fields, it was theorized by Rupp[25] that the gravity force density $F_{grav} = \rho g$ in equation 2.12 can be replaced by a magnetic force density term $F_{mag} = M\nabla B_0$ to yield the peak-to-peak distance λ:

$$\lambda = 2\pi\sqrt{\frac{\gamma}{M\nabla B_0}} \qquad \textit{Equation 2.14}$$

From this equation is it clear that the packing density of Rosensweig peaks increases as the gradient of the magnetic field is increased. Meyer found that this describes the peak-to-peak distance of a continuous pool of ferrofluid reasonably well[15]. However, as the translational freedom of a ferrofluid is limited, this equation may not hold any longer.

2.4 Spacecraft propulsion

The performance characteristics of a thruster are determined by two parameters: thrust and efficiency. In spacecraft, thrust T is provided by the expulsion of a propellant or combustion product at an effective exhaust velocity v_e and a mass flow rate $\dot{m}$[2]:

$$T = v_e\dot{m} = gI_{SP}\dot{m} \qquad \textit{Equation 2.15}$$

The effective exhaust velocity is given by the specific impulse I_{sp} and the Earth's gravitational acceleration g_0. The specific impulse is defined as the impulse (Newtons·s) provided per unit weight of propellant (Newtons) and is given in units of time. The higher the specific impulse of an engine is, the less propellant is needed to provide a certain amount of thrust and thus the more efficient the engine is. The other determining parameter for thrust is the mass flow rate, defined as the unit mass of propellant that is being expelled per second. Rocket engines have a poor specific impulse (250-450 s) but a very high mass flow rate (10-6000 kg/s), thus delivering a high amount of thrust. Electrospray thrusters on the other hand have a very high specific impulse (100-10000 s) but a very low mass flow rate (10^{-9}-10^{-4} kg/s) and thus provide a very low thrust.

For electric propulsion, the efficiency η of a thruster is given by the power of the electrospray jet P_j divided by the electrical input power P_{in}:

$$\eta = \frac{P_j}{P_{in}} = \frac{T^2}{2\dot{m}P_{in}} \qquad \textit{Equation 2.16}$$

Which, combined with equation 2.15, can be rewritten as the thrust-to-power ratio:

$$\frac{T}{P} = \frac{2\eta}{gI_{SP}} \qquad \textit{Equation 2.17}$$

The beam power is defined as the power from kinetic energy of the expelled ions or particles. The electrical power for satellites is supplied by solar panels and is usually the bottleneck for electric thrusters since it is dependent on the solar panel area and the solar flux, both of which are finite. From equation 2.16 and 2.17 it is evident that the efficiency is proportional to the specific impulse: a higher specific impulse means a more efficient engine and thus a longer lifetime. However, for a rocket engine with a constant efficiency there is a trade-off: the higher the specific impulse, the lower the thrust of the engine and thus the longer it takes to complete a trajectory change.

Assume a spacecraft flying in a circular orbit around the Earth with a constant velocity. In order to alter its trajectory to a wider orbit, the spacecraft requires a change in velocity (or delta-v) Δv, given by the total thrust on the spacecraft and the total spacecraft mass M:

$$\Delta v = \frac{T}{M} \qquad \textit{Equation 2.18}$$

The total spacecraft mass is given by the dry mass m_d and the propellant mass m_p. As the spacecraft performs an engine burn, the propellant mass decreases with the mass flow rate of the engine. Combining this with equation 2.15 and 2.18 gives:

$$\Delta v = -gI_{SP}\int_{m_d+m_p}^{m_d}\frac{dM}{M} = gI_{SP}\ln\frac{m_d+m_p}{m_d} \qquad \textit{Equation 2.19}$$

Equation 2.19, also known as the Tsiolkovsky rocket equation[26], illustrates how the specific impulse directly impacts the total life time of a satellite: if a satellite has a higher delta-v, it can adjust its slowly decaying orbit more often.

The specific impulse of an electrospray jet is determined by the effective exhaust velocity of the thruster, which in turn is given by the total exit velocity of all ions or charged particles that are emitted:

$$v_e = \sum v_i = \sum\sqrt{\frac{2q_iV}{m_i}} \qquad \textit{Equation 2.20}$$

Here, v_i is the exit velocity of a single ion or particle, q_i is the charge of the ion or particle, V is the acceleration voltage and m_i is the mass of the ion or particle. The specific impulse, and thus thrust, of an electrospray emitter can be adjusted by changing the mode in which the emitter is operating. If the emitter is in pure-ion mode, the charge-to-mass ratio is high and thus the specific impulse is higher, but thrust is lower. If it is operated in droplet mode, the charge-to-mass ratio is low and the specific impulse is lower, but thrust is higher. The emitter can also be operated in between these two modes, thus giving it a large operating range: it can have a specific impulse anywhere between 100 – 10000s and a thrust between 10^{-8} – 10^{-6} N[27]. This makes electrospray thrusters useful for a variety of missions, since they can be adjusted to meet the thrust or specific impulse requirements of the mission.

3. Experimental methods

3.1 ILFF array design

An ideal electrospray array consists of a support structure that is evenly spaced, densely packed and has a uniform height and shape[11]. A uniform height and shape are specifically important, because a thruster has to perform exactly as required to maintain the desired orbit. A strong, uniform magnetic field is required to obtain an ILFF electrospray array with these characteristics: the packing density of peaks is determined by the magnetic field strength and the uniform height and shape by the uniformity of the field. The best way to produce such a field is a large Helmholtz coil. Unfortunately, such a large Helmholtz coil is too big and heavy for a CubeSat, and would be a very substantial power drain on the satellite power supply. For this reason, permanent rare earth magnets are the preferred method for generating a magnetic field on small satellites. Rare earth magnets such as NdFeB magnets are compact, light and generate strong but non-uniform magnetic fields.

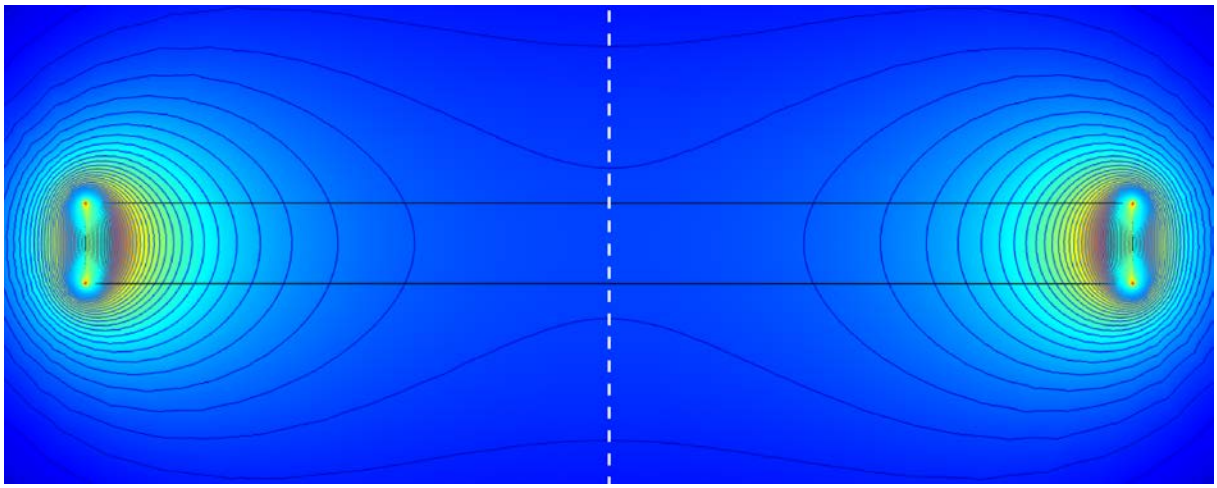

Figure 3.1: A COMSOL simulation of a grade N52 cylindrical magnet with thickness 6.35 mm and diameter 38.1 mm. The field is radially symmetric around the centre axis.

Figure 3.1 shows an image of the magnetic field lines and the intensity of the magnetic field of a grade N52 cylindrical magnet. The magnetic field lines diverge from the center of the magnet and loop around from the north pole to the south pole. The magnetic field is strongest near the sides of the magnet and quickly decreases further away from the magnet.

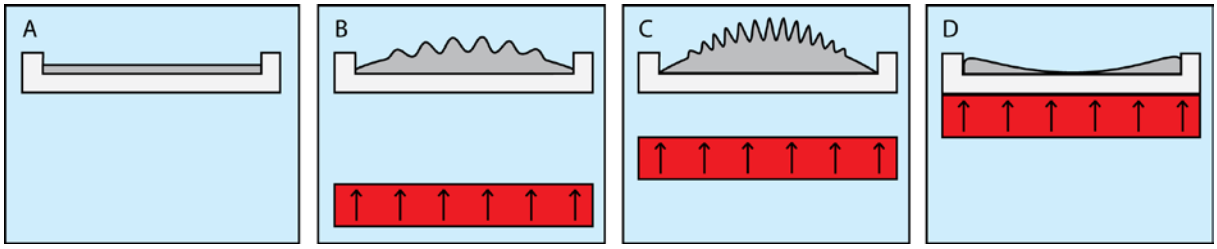

Figure 3.2: An illustration of a reservoir filled with ferrofluid above a permanent magnet shows how the fluid responds to the magnetic field. A) Without a magnetic field, the surface of the fluid is in rest. B) As a magnet is positioned underneath the reservoir, the fluid surface starts to bulge and big, widely spaced peaks appear. C) As the magnet is brought closer, the surface bulges further and the peaks become smaller and more closely spaced. D) If the magnet is brought very close, the ferrofluid is drawn to the sides of the magnet and the peaks disappear.

Figure 3.2 shows what happens if a reservoir of ferrofluid is placed far above the pole of a magnet and slowly brought closer to the magnet. As the ferrofluid comes closer to the magnet, the fluid surface starts to bulge and Rosensweig instabilities appear normal to the fluid surface. These instabilities start out as large, widely spaced peaks and become smaller and more densely packed as the ferrofluid experiences an increasingly stronger magnetic field. At a sufficiently close distance to the magnet, the ferrofluid is drawn to the sides of the magnet where the field is strongest and the instabilities disappear. For this reason, it seems preferable to use a magnet that is much wider than the ferrofluid reservoir: in the center of the magnet, the magnetic field is roughly uniform. However, a large magnet would introduce a high magnetic moment to the satellite. To prevent a satellite from aligning to the Earth magnetic field, the net magnetic moment of the satellite needs to be zero[28]. This can be accomplished by placing an identical magnet with opposite polarity at the other end of the satellite. The larger the thruster magnet is, the larger the counter magnet has to be. This makes the CubeSat too heavy and takes up too much space. Therefore a magnet that has a similar shape as the reservoir is preferable.

Figure 3.3: An illustration of various reservoir geometries: A) a circular pool, B) rectangular trenches and C) a ring trench.

The geometry of the ferrofluid reservoir is important: it limits the translational degree of freedom for the peaks. Since the support structure is a liquid, peaks can move and disappear and reappear at the edges. Figure 3.3 shows a schematic overview of several reservoir geometries. A circular pool of ferrofluid (Fig 3.3a) is unsuitable as an array for two reasons: the peaks are not of uniform height and shape (1) and peaks have a high translational degree of freedom (2). A rectangular trench reservoir filled with ferrofluid (Fig. 3.3b) with a small width ensures uniform height and shape for the peaks. It also limits the degree of freedom for the peaks, but does not stop the peaks from disappearing and reappearing at the edges. A ring reservoir with a small width (Fig. 3.3c) similar to the one Meyer used for his five-peak array ensures that all peaks are of uniform height and shape, limits their degree of freedom and prevents peaks from disappearing at edges. A ring design appears to be most favourable to form an array of evenly spaced Rosensweig peaks with uniform height and shape. The packing density in the ring can be tuned by changing the ring diameter, trench width and distance to the magnet.

The total number of peaks can be increased by increasing the number of rings. Creating a grid of small ring reservoirs with magnets underneath each reservoir is not an option: the magnetic fields of the magnets are altered by their neighbours. Instead, a design with concentric rings above a single magnet proved to be more efficient, but not optimal. Because the field is non-uniform, ferrofluid in the outer rings is drawn towards the sides of the magnet and the outer peaks do not have the desired shape and height. To circumvent this problem and modify the magnetic field of the magnet to be more uniform, a material with a high magnetic permeability can be introduced into the field. The material is magnetised, causing the magnetic field to change shape and intensity. This concept is used to shield sensitive electronics from magnetic fields.

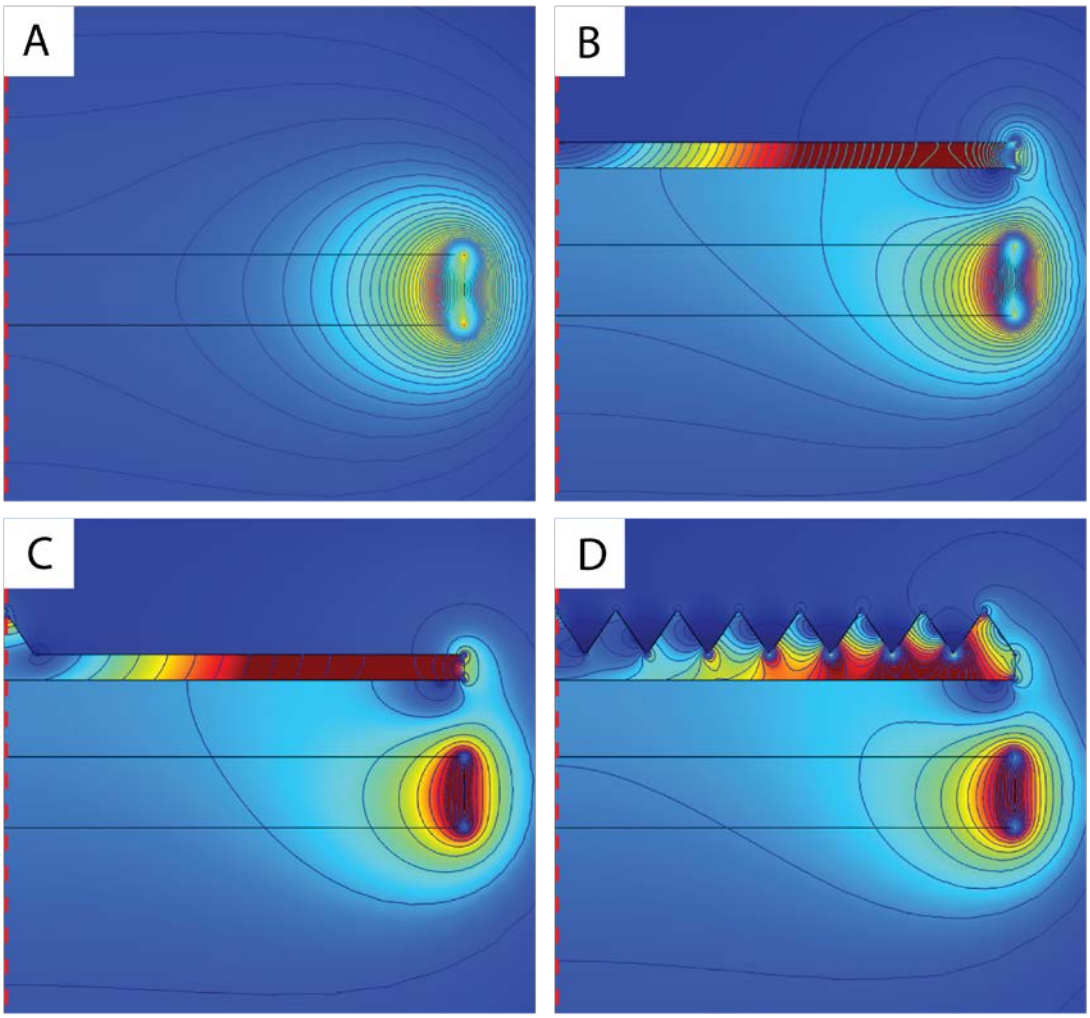

Figure 3.4: A COMSOL simulation of a grade N52 cylindrical magnet with thickness 6.35 mm and diameter 38.1 mm. The field is radially symmetric around the left axis. A) The magnetic field without any interfering objects. B) An iron plate is positioned above the magnet, altering the field. C) When a spike is introduced on the plate, a local intensity is present at the tip of the spike. D) The same effect is observed at the tips of ringed protrusions.

Figure 3.4 shows a COMSOL simulation of how the magnetic field generated by a cylindrical NdFeB magnet is altered by a plate of 99,99% Fe. When the magnet is surrounded by air (Fig. 3.4a), no alteration of the magnetic field is observed. However, as an iron plate is introduced parallel to the pole surface (Fig. 3.4b), the field strength above the plate is drastically decreased. When an iron plate with a protrusion at the centre is introduced (Fig. 3.4c), something interesting occurs: the magnetic field inside the plate is more intense at the tip of the protrusion. A similar effect is observed when a plate with ring protrusions is placed above the magnet (Fig. 3.4d): the field is not perfectly uniform, but is clearly more intense at the tip of the rings. Experiments confirmed that the field is more uniform when such an iron plate is placed above a

magnet: it was observed that the ILFF formed peaks at the tips of the protrusions, although the outer peaks still had a different shape than the inner peaks.

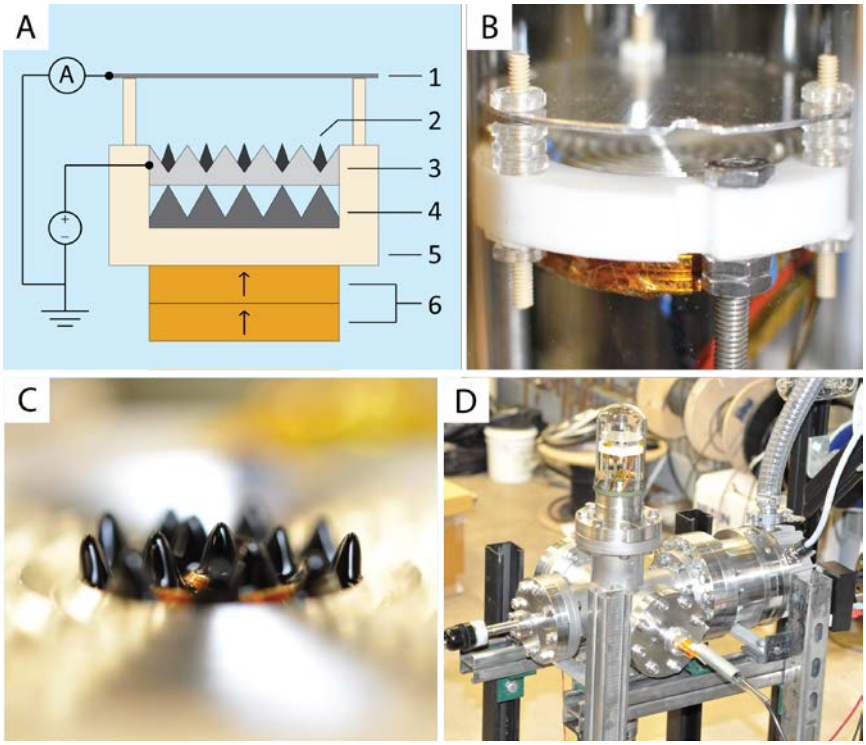

Figure 3.5: A) A schematic overview of the final design used for emission testing. (1) Extractor/collector plate, (2) ILFF, (3) aluminium reservoir, (4) iron plate, (5) Teflon base and (6) two N52 magnets. B) An image of the final design. C) An image of a typical array formed in the setup form B). D) The vacuum setup used in this project. The final design from B) is suspended on three threaded rods inside the domed viewport.

With the above results in mind, a final design as shown in Figure 3.5a and 3.5b was proposed. Concentric rings of depth 2.20 mm and width 2.54 mm were milled out of a 99.999% Fe cylindrical plate with thickness 6.35 mm and diameter 38.1 mm at a 60° angle. This iron plate was placed above two stacked cylindrical grade N52 NdFeB magnets with thickness 6.35 mm and diameter 38.1 mm with a Teflon spacer of thickness 6.35 mm in between the iron plate and the magnets. Concentric rings of depth 12.7 mm and width 2.54 mm were milled out of an aluminium ILFF reservoir at a 90° angle to further confine the ferrofluid above the iron plate protrusions. This aluminium reservoir was placed directly above the iron plate. This design proved reasonably effective at creating evenly spaced ILFF peaks of uniform shape and height (Fig. 3.5c), although peaks had a tendency to migrate to a neighbouring outer ring.

In order to perform I/V measurements, the aluminium reservoir was biased at negative polarity by connecting it to a high voltage power supply. The reservoir, iron plate and

magnets were encased in a Teflon base to prevent arcing between conductive components. The Teflon base was suspended on three threaded steel rods in the vacuum chamber. An aluminium extractor plate that doubled as a current collector was connected to a signal output wire and placed above the Teflon base at a variable distance by insulated threaded rods and screws.

3.2 Ionic liquid ferrofluid

The ILFF used in this project is a colloidal suspension of magnetic Fe_2O_3 nanoparticles sterically stabilised by poly($MAEP_{10}$-b-$DMAm_{60}$) in 1-ethyl-3-methylimidazolium bis(trifluoromethylsulphonyl)imide (EMIm-NTf2). The magnetic nanoparticles used for the synthesis were Fe_2O_3 particles provided by Sirtex Medical Limited. The block copolymer poly($MAEP_{10}$-b-$DMAm_{60}$) consists of monoacryloxyethyl phosphate (MAEP) and N,N-dimethylacrylamide (DMAm).

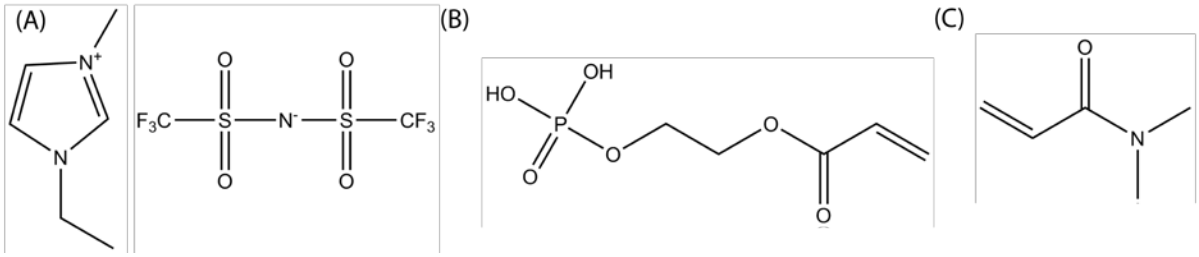

Figure 3.6: A) 1-ethyl-3-methylimidazolium bis(trifluoromethylsulphonyl)imide, B) monoacryloxyethyl phosphate and C) N,N-dimethylacrylamide.

Two different batches of ILFF were used in this project, which were based on EMIm-NTf2 and synthesised by Dr. Jain from the University of Sydney. They were prepared by mixing sterically stabilised magnetic nanoparticles dispersed in a 50:50 (w/w) water:ethanol mixture with EMIm-NTf2 followed by ultrasonification for 2 minutes. A more detailed description of the synthesis can be found in two previously published papers by Jain et al[14,29]. The concentrations of the two batches can be found in Table 3.1.

Batch	NJ397074	NJ397091A
Nanoparticles	Sirtex 102104	Sirtex
Fe_2O_3 w/w	26.3%	Unknown
EMIm-NTf2 (w/w)	3.9%	Unknown
Polymer (w/w)	69.8%	Unknown

Table 3.1: Concentrations of nanoparticles, ionic liquid and polymer in the two batches of ILFF that were used in this project.

3.3 Experimental setup

Vacuum setup and imaging

All I/V measurements were performed in a vacuum setup shown in Figure 3.5d. A six-way cross was used as a tank with two feedthrough flanges for high voltage input and signal output. The chamber was evacuated using a 110 L/min dry scroll pump and a 280 L/s turbomolecular pump, reaching a base pressure of 10^{-7} torr. The final array design as shown in Figure 3.5a was mounted on three threaded rods protruding from the base of the six-way cross. A domed viewport was placed around the array design to provide maximum visibility. All images of the electrospray setup were taken by a Nikon D5000 camera with an AF-S Micro Nikkor 60-mm f/2.8 ED lens.

Power supply and data acquisition

The voltage potential was supplied by a Glassman FC ±10 kV power supply that was set to negative polarity. The supply was connected to the aluminium fluid reservoir and grounded to the extraction electrode. The supply output was recorded in LabView using a USB-compatible data acquisition unit (DAQ). The signal current output from the extractor electrode was converted into a voltage signal by a transimpedance amplifier and recorded in LabView using a National Instruments DAQ.

4. Results

The second goal of this project was trying to achieve uniform emission from an ILFF electrospray array. In an attempt to quantify the emission from said array, a series of I/V measurements were performed with varying numbers of ILFF peaks. ILFF was injected into the aluminium reservoir via syringe while inside the magnetic field to obtain peaks of roughly equal height and shape. Each peak contained approximately 20 μL of ILFF. When the reservoir was filled before the magnetic field was applied, the resulting peaks did not become uniform in height or shape. This occurred because the fluid formed individual peaks instead of a continuous array of peaks. Changing the gradient of the magnetic field or increasing the reservoir depth and volume of ILFF in the reservoirs may remedy the non-uniformity of the peaks by creating a continous fluid. When filled, the inner sub reservoir contained a single peak, the first ring contained four peaks and the second ring contained seven to nine peaks. Peaks from different rings were found to have slightly different shapes due to the curvature of the rings. Initially, experiments were performed on a single peak and a five-peak setup with a Caen R1471ET ±5.5 kV power supply at a positive polarity.

It was found that a lot of arcing took place during testing between the reservoir, extractor plate, magnets and the three threaded suspension rods. These arcing events shorted the power supply, saturated the DAQ and essentially stopped the experiment. The power supply was switched to negative polarity, which slightly reduced the number of arcing events. Meyer also found that emission at negative bias voltage yielded much higher currents than emission at positive bias voltage[15]. A Glassman FX -10 kV power supply replaced the Caen RT1471ET to prevent shorting of the high voltage source during arcing events. The setup was better insulated, which eliminated all arcing events except those between the reservoir and extractor plate. It was determined that these arcs were caused by the formation of plasma in between the ILFF and the extractor plate. All tests described in this section were performed on twelve or thirteen-peak arrays.

4.1 Emission single peak

It was found that it was relatively simple to obtain emission from a single peak. While the peaks in the array were of roughly equal height, they were not perfectly identical and thus had different onset voltages. For each test, the tallest peak always had the lowest onset voltage and started emission first. It was attempted to quantify the emission of such a single ILFF emitter in order to determine the number of emitters in multi-peak tests by looking at the total emission current.

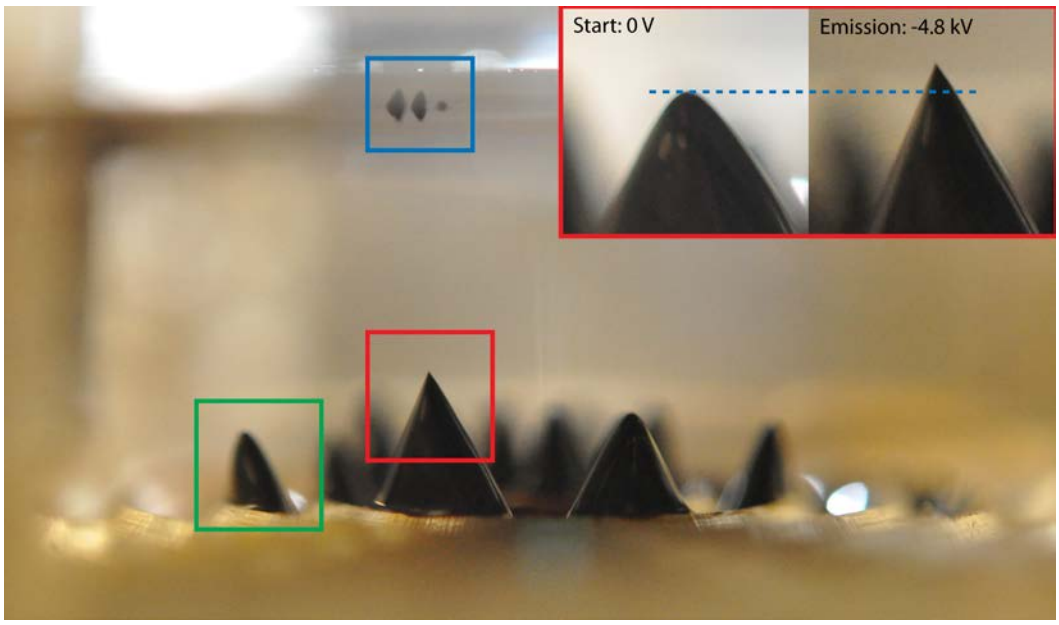

Figure 4.1: An image of a single ILFF emitter, highlighted in red. Note the height difference between peak at 0 V and at -4.8 kV. The emitted ILFF is collected on the extractor/collector plate and is highlighted in blue. One peak has migrated to an adjacent ring and is highlighted in green.

Figure 4.1 shows an image of a single ILFF emitter (designated Test 1) in the array. Rosensweig instabilities that are emitting can be identified by the sharp Taylor cone at the apex, as opposed to a regular rounded tip for non-emitting peaks. The ILFF that has been emitted by the peak (blue) is collected by the extractor/collector plate and is also exhibiting small Rosensweig instabilities due to the magnetic field. The extractor-reservoir distance was 9.56 mm in this experiment. None of the other peaks are emitting and one of the peaks has migrated to an adjacent ring (green).

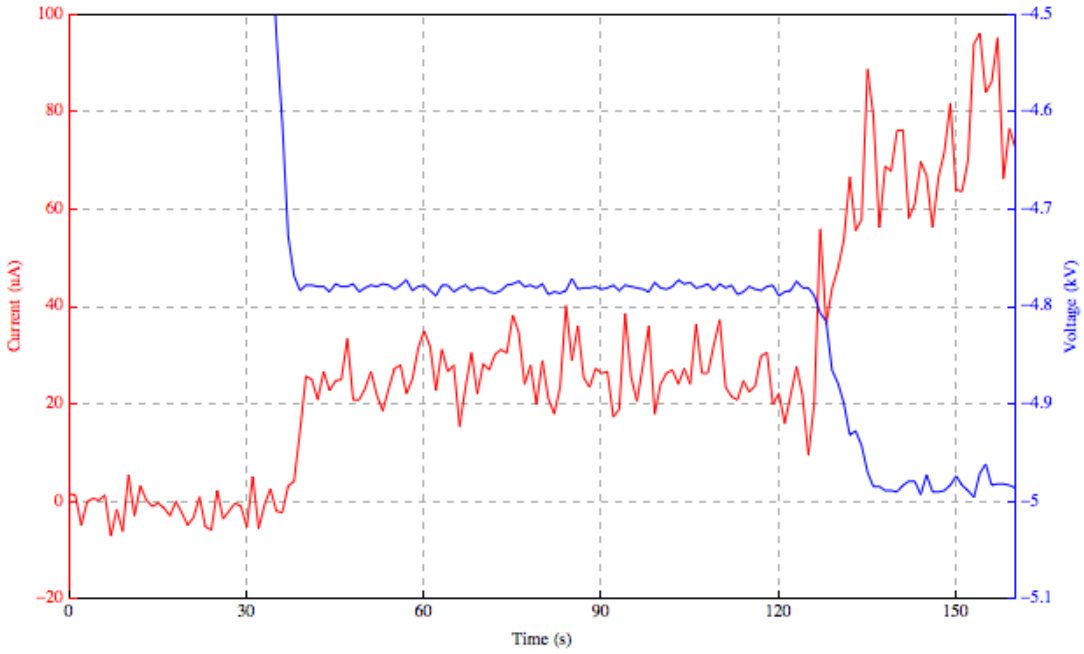

Figure 4.2: A current/voltage vs. time measurement of a single ILFF emitter. Red = current, blue = voltage. At the onset voltage of -4.8 kV, emission current is observed at 25-30 μA.

Figure 4.2 shows a graph of current/voltage vs. time of Test 1. The bias voltage was slowly ramped up until emission was observed around -4.8 kV, at which point the voltage was kept constant. The emission from a single emitter was found to be around 25-30 μA at the onset voltage. As the bias voltage was increased after some time, a sharp increase in emission current was also observed until an arcing event saturated the DAQ unit and ended the test. None of the other peaks in the array showed emission during this test. Because the emission current of an emitter increases with increasing voltage, it is not possible to accurately determine the number of emitters unless all peaks start emission at the same onset voltage.

4.2 Emission four-peak array

In multiple experiments, confirmed emission from more than a single peak was observed, especially at higher voltages. Unfortunately, fatal arcing events took place more frequently at high voltages, rendering many current/voltage measurements useless. Figure 4.3 shows a current/voltage vs. time measurement of an array of twelve peaks, designated Test 2. The extractor-reservoir distance during this experiment was 5.8 mm. As the bias voltage was increased, emission from a single peak was observed at an onset voltage of around -4.6 kV; the bias voltage was kept constant at this value. During the first 20 seconds of emission, an emission current of 25-30 μA was observed.

The power supply was found to shut down for very short instances during the entire test. When this happened the emission current dropped to zero, after which it increased to the old value. After roughly 20 seconds of emission from the single peak the current suddenly increased to around 200 µA and started fluctuating ±50 µA. From this point onwards, continuous emission was observed from four Rosensweig instabilities, as can be seen in Figure 4.4. At t = 2 min, the bias voltage was further increased to -4.8 kV and kept constant for 150 seconds. As the voltage was increased, the emission current rose to 500 µA and fluctuated heavily with ±100 µA. While the voltage was kept constant, the emission current slowly decreased to 200 µA with occasional spikes, until the voltage was switched off and emission stopped. While all four peaks appeared to have an onset voltage of -4.6 kV or lower, initially only one peak started emitting. The delay of the other three peaks may be caused by redistribution of the fluid in the outer ring of the reservoir in which they were located. The high fluctuations that started around t = 1 min may be caused by periodic emission from any peaks other than the original four peaks.

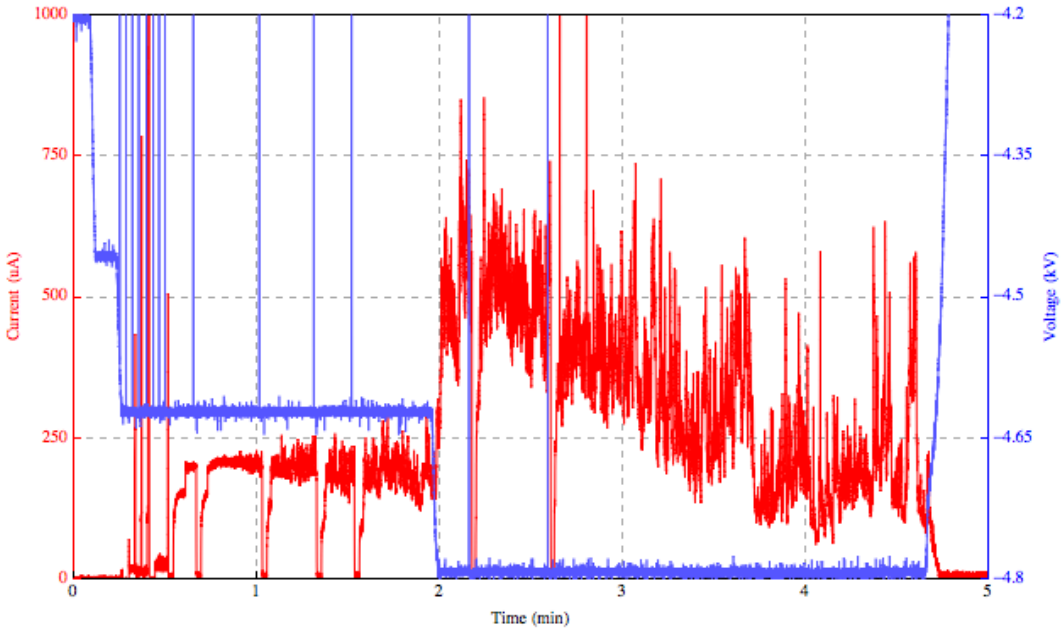

Figure 4.3: A current/voltage vs. time measurement of an array of twelve ILFF peaks. Red = current, blue = bias voltage. At t=20s, emission starts from a single peak. At t=40s, three additional peaks start emitting. After the voltage is increased to -4.8 kV and kept constant, the emission current slowly decays from 500 µA to 200 µA.

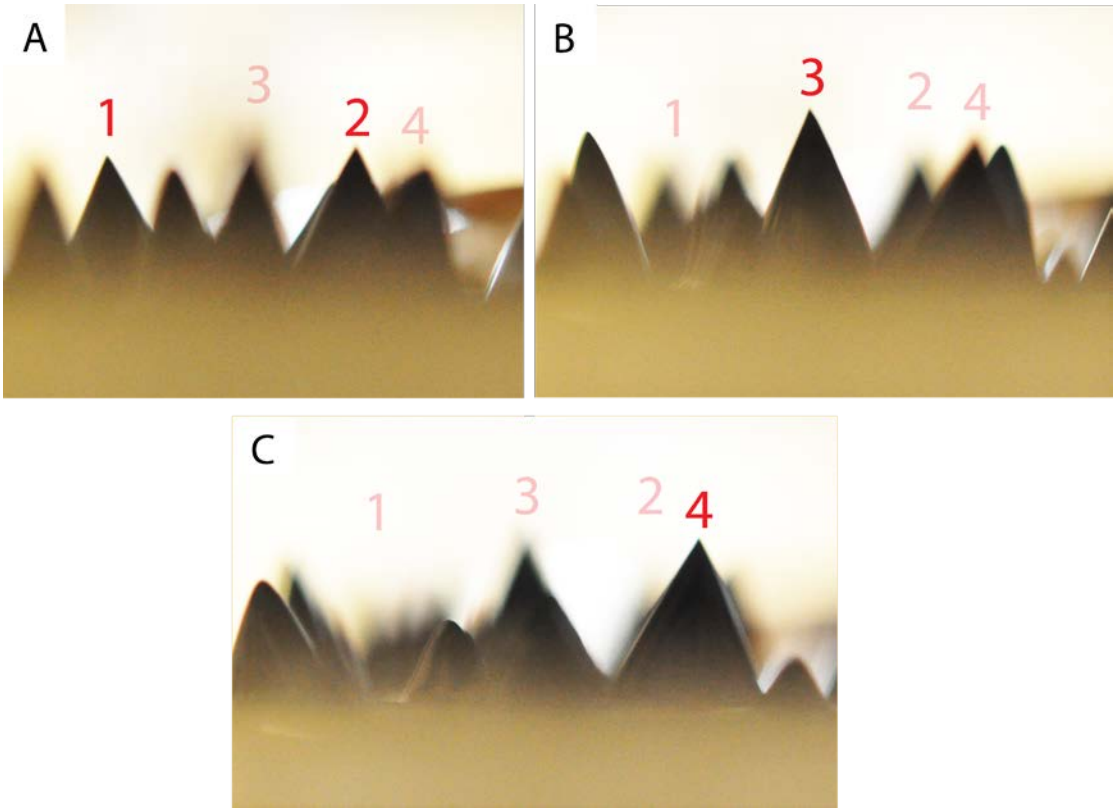

Figure 4.4: Emission observed from four peaks in the array at different focus lengths.

4.3 Emission seven- and eight-peak array

In a few experiments, emission was observed from more than five peaks. Such experiments were usually accompanied by the formation of plasma and many arcing events, some of them fatal for the experiment. Figure 4.5 shows a current/voltage vs. time measurement of a twelve-peak array (designated Test 3). The extractor-reservoir distance was 5.8 mm during this experiment. The onset voltage of the first peak(s) was -4.3 kV. The bias voltage was kept constant at -4.4 kV and an emission current of 150 μA was observed. The power supply shorted several times, removing the voltage potential for very short instances and causing emission to stop and restart. After one of these shorts at t = 20 s, the emission current increased to 400 μA for a few seconds after which a fatal arcing event took place. The emission current did not fluctuate much compared to Figure 4.3, 'only' ± 50 μA. No formation of plasma was observed during this test.

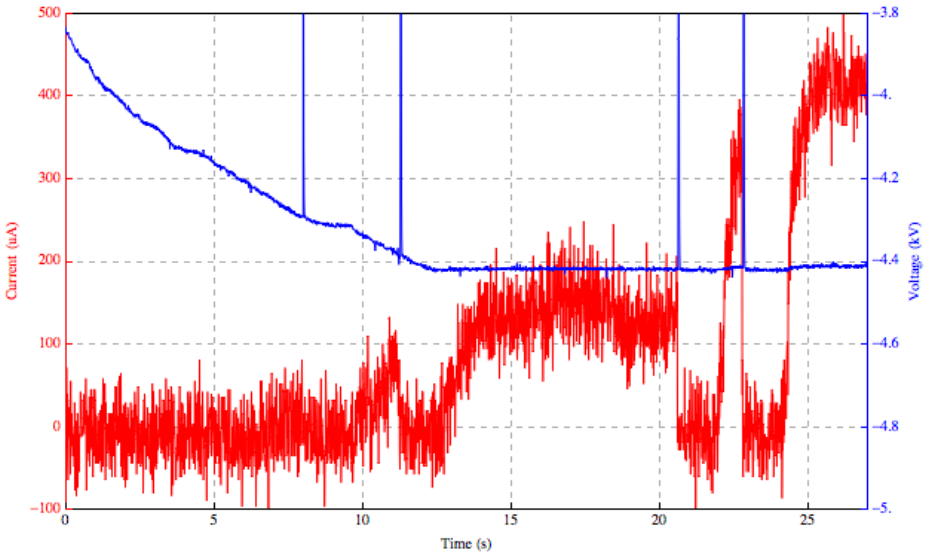

Figure 4.5: A current/voltage vs. time measurement of an array of twelve ILFF peaks. Red = current, blue = bias voltage. The bias voltage was kept constant at -4.4 kV. At t=10s, emission starts. At t=25s, a sharp increase in current marks the onset of emission for additional peaks.

After inspection of the extractor/collector plate at the end of the test, it was found that it had seven ILFF spots on it; indicating that seven peaks achieved emission. Figure 4.6 shows the array before testing and the extractor/collector plate after testing. The size of the spots is an indication of how long a peak has been emitting; the bigger the spot, the longer the peak has emitted. From this it can be concluded that emission mainly took place from the outer ring, and that the middle peak was last to emit. No emission was obtained from the second ring; most likely because these peaks were either lower or have a different radius of curvature at the tip. Important to note is that the emission was fairly uniform and did not fluctuate much, albeit that the test only lasted 27 seconds.

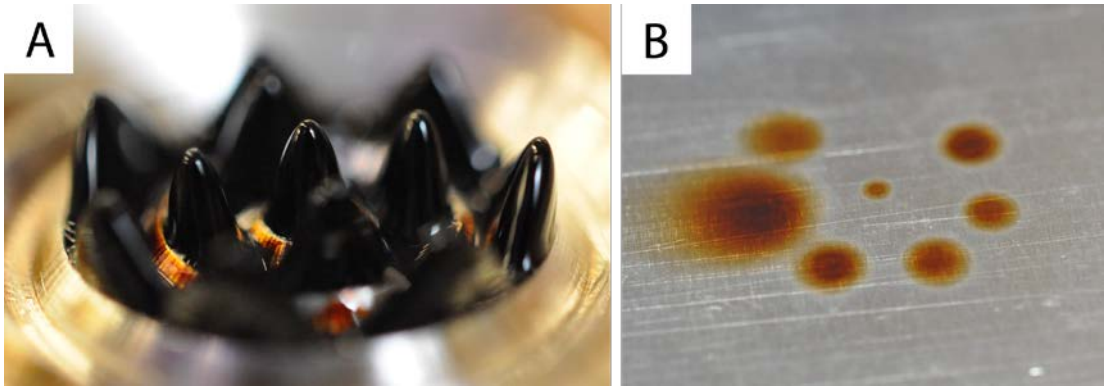

Figure 4.6: A) An array of twelve peaks before testing. B) After testing, seven spots of ILFF were found on the extractor/collector plate, evidence that seven peaks were emitting during the test. The size of the spot is probably an indication for how long the peak has been emitting.

In another experiment (Test 5), emission was observed from eight peaks in an array of thirteen peaks. The bias voltage was set to -3.48 kV after the onset of emission was found to be -3.43 kV with an extractor-reservoir distance of 5.8 mm. Numerous fatal arcing events took place during this test, rendering any current/voltage measurements useless. Figure 4.7 shows the extractor/collector plate after testing. Eight spots of carbonised ILFF are visible, seven of which correspond to emission from peaks in the outer ring. This may be because peaks in different rings have slightly different shapes due to varying radii of curvature of the rings.

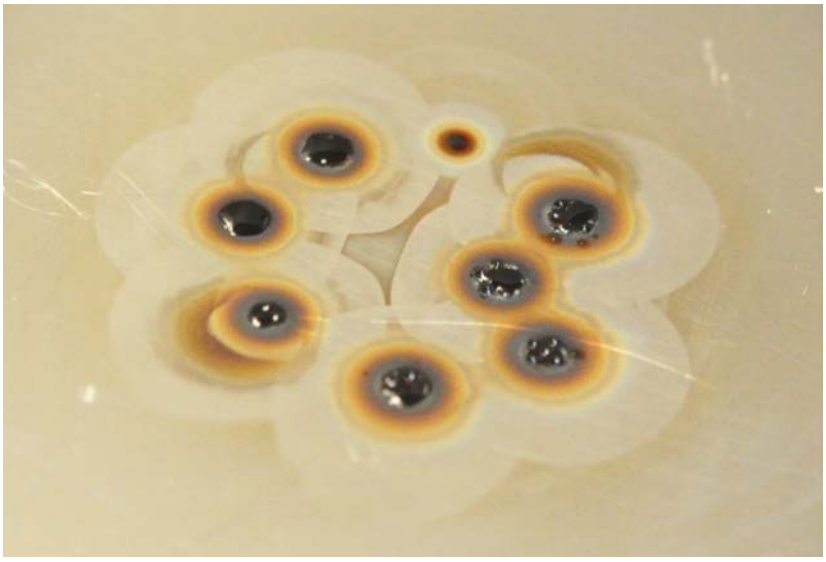

Figure 4.7: An image of the extractor/collector plate after Test 5 emission measurements on a thirteen-peak array. Eight carbonised black spots are visible, evidence that emission was obtained from eight ILFF peaks. Seven spots have roughly the same size, indicating that emission was from the peaks was fairly uniform.

Seven spots are roughly of equal size, indicating that these peaks started emitting at roughly the same time and rate. The average diameter of the dark spots is 4.18 mm. From images, it was estimated that the peak height was roughly 3 mm. Basic geometry yields a maximum beam angle of approximately 34.84°. The majority of ions or particles emitted are most likely in the centre of the beam, since a gradient in thickness can be observed for the spots.

4.4 Other observations

In some experiments, a slow decay was observed in emission current over time, especially if the ILFF had been used in a test before. Figure 4.8 shows current/voltage vs. time measurement Test 6 from the same array that was used in Test 5. The onset voltage was found to be much higher than during the previous test: -4.8 kV as opposed to -3.43

kV. There are two possible explanations for this: depletion of the fluid and/or deterioration of the reservoir fluid. The reservoir fluid is not being replenished during tests, meaning that the peaks become smaller as they emit. As this happens, the peak-to-extractor distance increases and the onset voltage becomes higher.

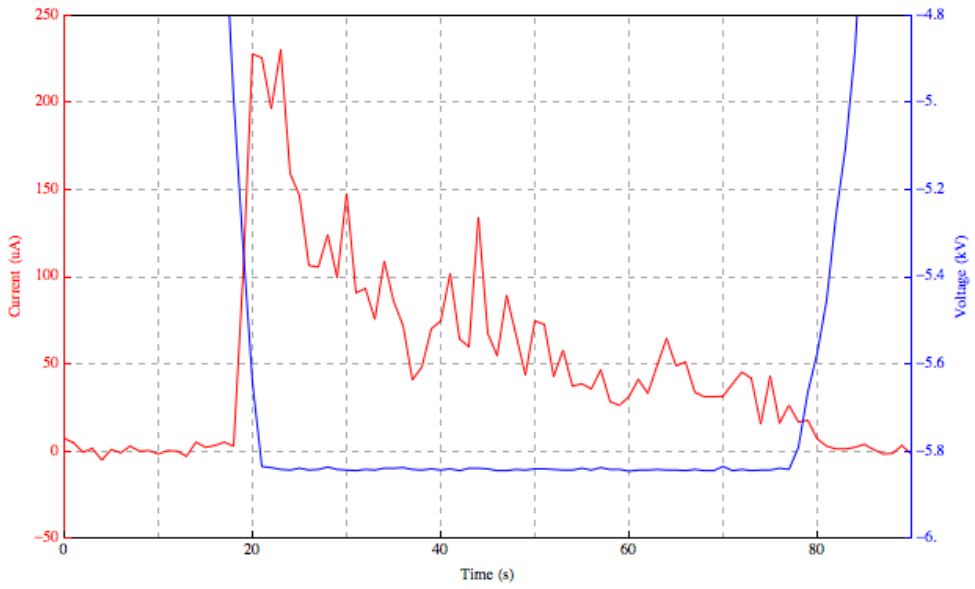

Figure 4.8: A current/voltage vs. time measurement of the thirteen-peak array after Test 5. Onset of emission is at -4.8 kV. The bias voltage was kept constant at -5.8 kV, during which time the emission decayed from 200 μA to 25 μA.

The ILFF that is emitted is dark and still responds to a magnetic field, indicating that both EMIm-NTf2 and nanoparticles were being emitted and that the array was in mixed or droplet-mode. The leftover fluid recovered after testing was found to be more viscous than before testing. This is most likely because proportionally more EMIm-NTf2 is being emitted than nanoparticles, causing the reservoir fluid to become more viscous. As the ratio of IL-to-nanoparticles changes, the physical properties of the fluid such as surface tension and magnetization also change. This may cause the ILFF to respond differently to the magnetic and electric fields. If ILFF would be used as a thruster, the reservoir would be replenished. Adding fuel that has a higher IL-to-nanoparticles ratio to the reservoir may compensate for the proportional loss of EMIm-NTf2.

Plasma formation was observed in multiple experiments and was usually accompanied by a high frequency (1-10 per second) of arcing events. It occurred more often at higher bias voltages. Figure 4.9A shows an image of a twelve-peak array during emission measurement Test 7 at -5 kV. Plasma can be seen on the right side of the array as a

purple-blue haze. Plasma slowly built up during testing until a critical density was reached and an arc could be observed between the reservoir and the extractor/collector plate. Sometimes, these arcs were fatal and ended the test. The formation of plasma may be prevented by creating smaller arrays that have a smaller reservoir-extractor distance and thus have a lower onset voltage. Separating the extractor and collector plates may help to prevent fatal arcing events to the current collector. Allowing the plasma to vent better by having more free space around the setup may also help. Figure 4.9B shows the extractor plate after testing, on which several spots of carbonised ILFF can be observed. The carbonisation may have caused by local high current density due to arcing.

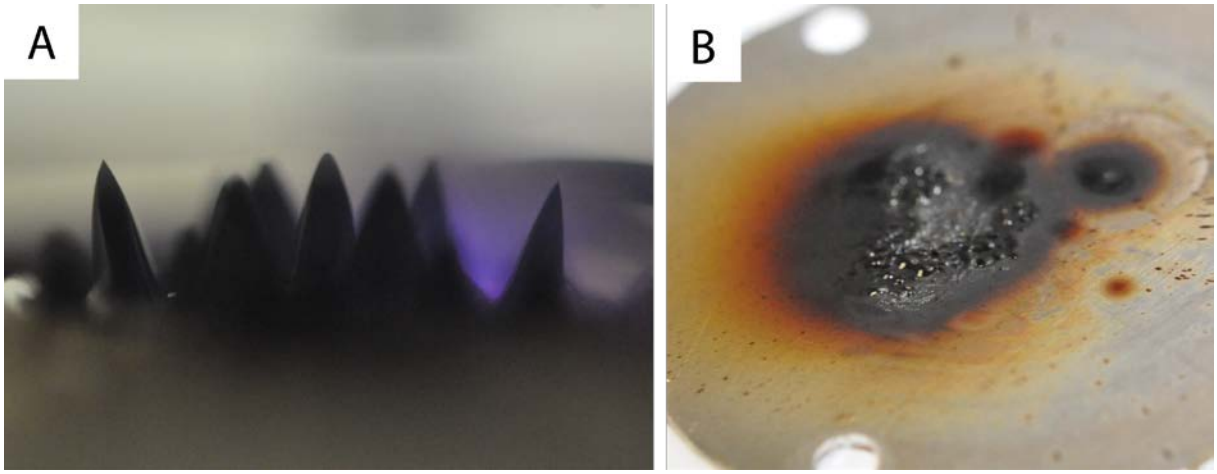

Figure 4.9:A) An image of an array during Test 7. Several peaks show Taylor cones and are emitting. Plasma formation can be seen on the right side of the array as a purple-blue haze. B) The extractor plate after testing. Carbonised ILFF is clearly visible.

Figure 4.10 shows current/voltage vs. time measurement Test 7. Onset of emission was at -4.9 kV, the bias voltage was kept constant at -5 kV. The emission current behaved very erratic: it increased slowly from ±75 µA to 400 µA, but showed spikes up to 600 µA. The test was ended by a fatal arcing event.

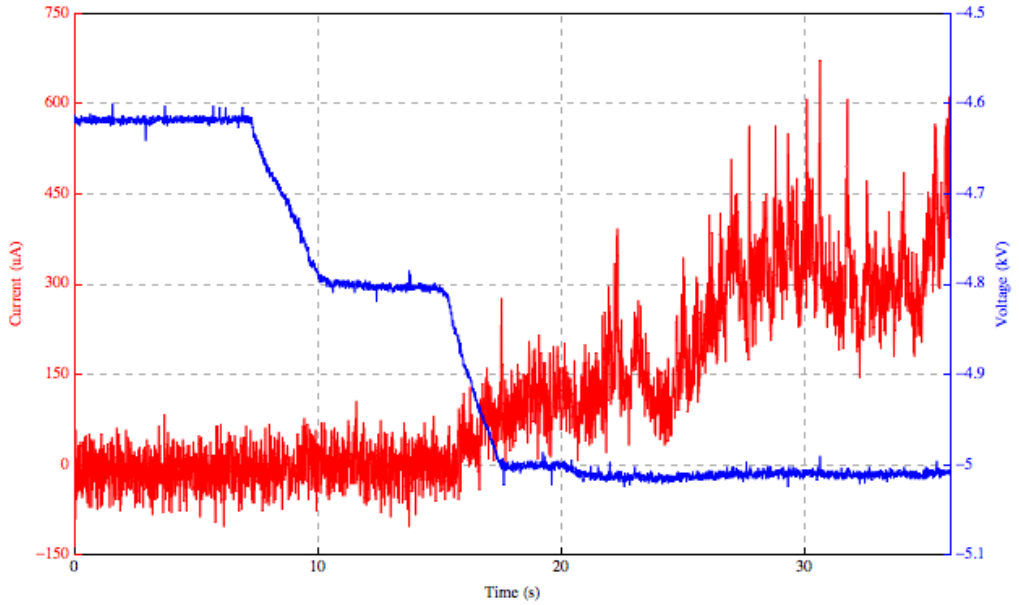

Figure 4.10: A current/voltage vs. time measurement of a twelve-peak array during Test 7. Onset of emission was at -4.9 kV. The emission current was very erratic and spiked up to 600 μA before an arcing event ended the test.

5. Conclusion

The goal of this project was to design and build a working multi peak ILFF emitter array and identifying any difficulties in building and operating such an array. The goal was divided into two sub goals: 1) designing and building a multi-peak array setup and 2) achieving uniform electrospray from this array.

5.1 Design and construction of a multi-peak array

It was found that a circular reservoir with a pool of ILFF was not the optimal design for an array of uniform Rosensweig instabilities, even though this provides the highest peak density. A reservoir design with concentric ring trenches provided the highest control over peak shape and height. To circumvent the problem of a non-uniform magnetic field, an iron plate with protrusions was placed between the magnet and the reservoir, so that the magnetic field was locally stronger underneath each of the rings. This final designed proved reasonably effective at creating an array of twelve to fourteen peaks, but it was found that the peaks in different rings had slightly different shapes due to the curvature of the rings. Because the ferrofluid formed non-continuous peaks, it was found that it was very tedious to create a uniform array, as each peaks had to be individually injected.

5.2 Emission experiments

Obtaining uniform emission from an array of peaks proved to be difficult due to two reasons. Firstly, the peaks in the array proved to be too non-uniform: a small difference in height yielded different onset voltages for different peaks and thus different emission intensities at a given bias potential. Secondly, experiments were hindered by arcing events that saturated the DAQ-unit used to record the current and essentially ended the test. Most arcing events were due to the formation of plasma in between the extractor/collector plate and the reservoir. However, it was observed that relatively uniform emission was achieved in some experiments, usually from peaks in the same reservoir ring. In some experiments a slow decay in emission current was observed over time, most likely due to depletion or deterioration of the reservoir fluid.

6. Outlook

In order to obtain uniform emission from a dense array of uniform peaks, several areas of improvement are recommended for the current array design. Firstly, making the ring reservoirs deeper and tuning the magnetic field gradient may yield a more continuous reservoir fluid, which would benefit the uniformity of peaks. Secondly, custom magnets may prove better suited to create a uniform array. Changing the geometry of the magnets by creating tapered ends or adding a grid of spikes at the poles may make the magnetic field more uniform. Thirdly, (fatal) arcing events should be eliminated by preventing the formation of plasma. This may be achieved by separating the extractor and collector plates to allow the plasma to vent away from the array. Finally, alternate designs should remain subject of investigation, since having a delicate array of spikes protrusions defeats the purpose of having the ILFF form its own support structure. By trying to create a more uniform magnetic field, a pool of ILFF may yield a high-density array of uniform peaks.

Another area of investigation is determining the composition of the emitted fluid. It was found that the reservoir fluid became more viscous after testing, indicating that the IL-to-nanoparticle ratio decreased. This may cause a change in fluid properties, which may affect the performance of an ILFF electrospray thruster. In order to be considered as a thruster, the emission characteristics such as charge-to-mass ratio, mass flow and IL-to-nanoparticles ratio must be well known.

References

1: Toorian, A., Diax, K., and Lee, S. The CubeSat Approach to Space Access. *IEEE Aerospace Conference, Big Sky, MT* (2008)

2: Goebel, D. and Katz, I., Fundamentals of Electric Propulsion: Ion and Hall Thrusters. *John Wiley and Sons, Inc., Hoboken, New Jersey,* (2008)

3: Seiferts et al. Propulsion for Nanosatellites. *32nd International Electric Propulsion Conference, Wiesbaden, Germany*, (2011)

4: Noon et al. The Ion Propulsion System for Dawn, *AIAA 2003-4542, 39th Joint Propulsion Conference, Huntsville, Alabama*, (2003)

5: P. Shaw. Pulsed Plasma Thrusters for Small Satellites. *PhD thesis, University of Surrey* (2011)

6: Gibbon, D., Baker, A., Coxhill, I. and Sweeting, M. The Development of a Family of Resistojet Thruster Propulsion Systems for Small Spacecraft. *17th Annual AIAA/USU Conference on Small Satellites*

7: Li, H., Courtney, D., Diaz Gomez Maqueo, P. and Lozano, P. Fabrication and Testing of an Ionic Electrospray Propulsion System with a Porous Metal Tip Array. *Solid-State Sensors, Actuators and Microsystems Conference (TRANSDUCERS), Beijing, China* (2001)

8: Gassend, B. , Velásquez-García, L., Akinwande, A. and Martínez-Sánchez, M. A Fully Integrated Microfabricated Externally Wetted Electrospray Thruster. *43rd AIAA/ASME/SAE/ASEE Joint Propulsion Conference, Cincinnati* (2007)

9: Gamero-Castano, M.; Hruby, V. Electrospray as a source of nanoparticles for efficient colloid thrusters. *J. Propul. Power, 17, 977-987* (2001)

10: Chiu, Y., Austin, B. and Dressler, R. Mass Spectrometric Analysis of Colloid Thruster Ion Emission from Selected Propellants. *Journal of Propulsion and Power, 21(3):416–423* (2005)

11: Paulo Lozano. Studies on the Ion-Droplet Mixed Regime in Colloid Thrusters. *PhD thesis, MIT* (2003)

12: Dandavino, S., Ataman, C., Shea H., Ryan, C. and Stark J. Microfabrication of Capillary Electrospray Emitters and ToF Characterization of the Emitted Beam. *The 32nd International Electric Propulsion Conference, Wiesbaden, Germany* (2011)

13: Courtney, D., Li, H. and Lozano, P. Electrochemical Micromachining onPorous Nickel for Arrays of Electrospray Ion Emitters. *Journal of Microelectromechanical Systems, 22(2):471–182* (2013)

14: King, L., Meyer, E., Hopkins, M., Hawkett, B. and Jain, N. Self-Assembling Array of Magnetoelectrostatic Jets from the Surface of a Superparamagnetic Ionic Liquid. *Langmuir*, 2014.

15: Meyer, E. Development of an Ionic Liquid Ferrofluid Electrospray Source and Mode Shape Studies of a Ferrofluid in a Non-uniform Magnetic Field. *PhD thesis, MTU* (2014)

16: Diderot, D. Encyclopédie, ou dictionnaire raisonné des sciences, des arts et des metiers. *Paris* (1751-1772)

17: Zeleny, J. The Electrical Discharge from Liquid Points, and a Hydrostatic Method of Measuring the Electric Intensity at their Surfaces. *Physical Review, 3(2):69–91* (1914)

18: Taylor, G. Disintegration of Water Drops in an Electric Field. *Proceedings of the Royal Society of London, 280(1382):383–397* (1964)

19: Maher, S., Jjunju, F. and Taylor, S. 100 years of mass spectrometry: Perspectives and future trends. *Rev. Mod. Phys. 87, 113* (2015)

20: Huanga, Z., Zhangb, Y., Kotakic, M. and Ramakrishna, S. A review on polymer nanofibers by electrospinning and their applications in nanocomposites. *Composites Science and Technology, 63, 2223-2253* (2003)

21: P.D. Prewett and G.L.R Mair. Focused Ion Beams from Liquid Metal Ion Sources. *Research Studies Press LTD., Somerset, England* (1991)

22: Raj, K., Moskowitz, B., Casciari, R. Advances in ferrofluid technology. *Journal of Magnetism and Magnetic Materials, 149, 174-180* (1995)

23: Jain, N., Zhang, X., Hawkett, B. and Warr, G. Stable and Water-Tolerant Ionic Liquid Ferrofluids. *ACS Appl. Mater. Interfaces, 3, 662-667* (2011)

24: Rosensweig, R. Ferrohydrodynamics. *Cambridge University Press* (1985)

25: Rupp, P. Spatio-temporal Phenomena in a Ring of Ferrofluid Spikes. *PhD thesis, University of Bayreuth* (2003)

26: Tsiolkovsky, K. Исследование мировых пространств реактивными приборами (The Exploration of Cosmic Space by Means of Reaction Devices), *The Science Review* (1903)

27: Ziemer, J. Performance of Electrospray Thrusters. *31st International Electric Propulsion Conference, Ann Arbor, MI* (2009)

28: Inamori, T., Sako, N. and Nakasuka, S. Magnetic dipole moment estimation and compensation for an accurate attitude control in nano-satellite missions. *Acta Astronautica, 68, 2038-2046* (2011)

29: Hawkett et al. The composition and end-group functionality of sterically stabilized nanoparticles enhances the effectiveness of co-administered cytotoxins. *Biomater. Sci., 1, 1260–1272* (2013)